

# WHAT FRACTION OF THE YOUNG CLUSTERS IN THE ANTENNAE GALAXIES ARE “MISSING” <sup>1</sup>?

BRADLEY C. WHITMORE & QING ZHANG<sup>2</sup>

Space Telescope Science Institute, 3700 San Martin Drive, Baltimore, MD 21218

Electronic mail: whitmore@stsci.edu

Received:

<sup>1</sup> Based on observations with the NASA/ESA *Hubble Space Telescope*, obtained at the Space Telescope Science Institute, which is operated by the Association of Universities for Research in Astronomy, Inc., under NASA contract NAS5-26555.

<sup>2</sup> Also Johns Hopkins University, 3700 San Martin Drive, Dept. of Physics & Astronomy , Baltimore, MD, 21218.

## ABSTRACT

A reexamination of the correspondence between 6 cm radio continuum sources and young star clusters in the Antennae galaxies indicates that  $\sim 85\%$  of the strong thermal sources have optical counterparts, once the optical image is shifted  $1''.2$  to the southwest. A sample of 37 radio-optical matches are studied in detail showing correlations between radio properties (i.e., total flux and spectral index) and a variety of optical characteristics (i.e., intrinsic cluster brightness,  $H\alpha$  flux and equivalent width, extinction, and cluster ages). There is a strong correlation between the radio flux and the intrinsic optical brightness. In particular, the brightest radio source is also the intrinsically brightest optical cluster (WS80). It is also the most extinguished cluster in the sample, the strongest CO source and the strongest 15 micron source. Furthermore, the brightest ten radio sources are all amongst the youngest clusters with ages in the range 0 - 4 Myr and extinctions from  $A_V = 0.5$  to 7.6 mag (with a median value of 2.6 mag). A weak correlation between age and  $A_V$  suggests that  $\sim 6$  Myr are typically required to remove enough dust to reach  $A_V = 1$  mag. The radio-bright phase lasts only about 10 Myr in these clusters, consistent with the interpretation that most of the radio emission originates from hot gas. Many of the non-detections are probably individual supernova remnants since they have relatively steep radio indices typical of non-thermal sources. Only a few of the very red clusters originally discovered by Whitmore & Schweizer are radio sources, contrary to earlier suggestions. Finally, a new hybrid method of determining cluster ages has been developed using both UBVI colors and  $H\alpha$  equivalent widths to break the age-reddening degeneracy. We find that the Bruzual & Charlot models, which use the Padova spectral evolution tracks, fit the data reasonably well while the Leitherer &

Heckman models, using the Geneva tracks, have a large red loop for ages 8 - 13 Myr that does not agree with the data.

Key Words: galaxies: star clusters, galaxies: interactions, galaxies: individual (NGC 4038/4039)

## 1. INTRODUCTION

Star formation requires an ample reservoir of cool molecular gas as raw material. Along with the gas comes dust, resulting in the ironic situation that many of the brightest stars cannot be seen in the optical due to obscuration by dust. Fortunately, radio and infrared observations are able to penetrate much of the dust, providing a window into the star formation process. This is important for two basic reasons: 1) it allows us to observe the stars using many different wavelengths, thus providing better diagnostics for unraveling the processes involved in star formation, 2) it allows us to determine whether conclusions based on an incomplete census of optical sources are jeopardized by incompleteness.

Merging galaxies are the sites of the most active star formation in the universe. The Antennae Galaxies (NGC 4038/39) represent perhaps our best chance to study the process in detail, since they are both the youngest and nearest galaxy in Toomre’s (1977) list of 11 prototypical mergers. Whitmore et al. (1999) have identified a rich population of young compact star clusters in the Antennae, many of which have all the attributes expected of young globular clusters. The “overlap” region between the two galaxies is the site of the most active star and cluster formation in the system. Unfortunately, the extensive dust in this region makes it difficult to study the clusters in detail. Several authors have highlighted the close connection between the clusters, infrared sources (Vigroux et al. 1996), sources of CO emission (Wilson et al. 2000), and a variety of sources observed in other wavelengths (Zhang, Fall, & Whitmore 2001). However, other authors have stressed the difficulties of penetrating the dust, and have concluded that most of the sites of star formation may

actually be embedded in optically thick layers of dust with  $A_V \sim 70$  (Kunze et al. 1996, Mirabel et al. 1998). For example, Neff and Ulvestad (2000) state that “The strongest radio continuum emission occurs between the galaxies, at an optically unremarkable location near but not coincident with an extremely red cluster detected by Whitmore & Schweizer.”

In this paper we reexamine the question of whether most of the strong radio sources are actually missing from the optical survey of young clusters, due to extinction from dust. We adopt a Hubble Constant of  $H_0 = 75 \text{ km s}^{-1} \text{ Mpc}^{-1}$ , which places NGC 4038/4039 at a distance of 19.2 Mpc, corresponding to a distance modulus of 31.41 mag. At this distance, the projected scale is  $1'' = 93 \text{ pc}$ , and 1 pixel on the Planetary Camera covers 4.23 pc while one pixel on the Wide Field Camera covers 9.26 pc.

## 2. A COMPARISON BETWEEN RADIO AND OPTICAL POSITIONS

### *2.1 Statistical Analysis*

Accurate coordinates are the primary requisite for the identification of optical counterparts to radio and IR sources. This requires both high spatial resolution, in order to pinpoint a given target, and an accurate absolute reference frame shared by the two observations. The spatial resolution for the available IR observations in the Antennae is roughly  $2''$  (Mirabel et al. 1998). While this is good enough to establish the fact that many of the IR sources have optical counterparts (Vigroux et al. 1996, Mirabel et al. 1998), it is difficult to make precise comparisons since there are often several optical sources within a search radius. The radio observations from Neff & Ulvestad (2000) provide much better positional accuracies, with uncertainties  $\sim 0''.4$ , based on a comparison of their 6 and 4 cm positions

for the same cluster (note that the 6 cm positions are used for comparisons in the present paper). HST observations have *relative* accuracies  $\sim 0.1''$  (Voit 1997). Unfortunately, the absolute uncertainties of the HST positions are much larger, typically  $\sim 1''$  (Biretta et al. 2001), due to uncertainties in the absolute positions of the guide stars. Hence, an offset of 1 - 2'' should be considered when making positional matches with HST data.

Figure 1 (*bottom*) shows the positions of the nine bright (i.e., radio flux  $S \geq 70 \mu\text{Jy}$ ), thermal (i.e., radio index  $\alpha \geq -0.4$ , where  $\alpha$  is defined by  $S_\nu \propto \nu^{+\alpha}$ ), 6 cm radio sources that fall in the overlap region of the Antennae (Neff & Ulvestad 2000, Table 5). We begin our comparison using this subset of the 109 radio sources because they are the most likely to have optical counterparts, based on the fact that similar sources in the Milky Way are often associated with compact HII regions.

Neff & Ulvestad (2000) found that many of the radio sources are near, but not coincident with optical sources. They suggest that the true counterparts are embedded in dust, and are not observed in the optical passbands. However, we note from Figure 1 (*bottom*) that the nearest optical candidates are generally seen toward the northeast, hence a common offset may bring the radio and optical positions into agreement. The result of adding a  $1''.2$  offset toward the southwest is shown in Figure (*top*).

We now find that eight of the nine radio sources have optical counterparts (defined as point-like sources from Whitmore et al. 1999 with  $M_I < -9.0$ ) which are within  $0''.5$  of the radio positions. Without the offset, only three of the radio sources would have matches given the same criteria, which is roughly what would be expected for a random distribution

(see Figure 2 and discussion below).

If we expand the field of view to include the full HST image we find a similar story, with matches for 11 of the 13 bright thermal radio sources using the  $1''.2$  offset. Using no offset yields only 3 of 13 matches. The chances of matching 11 out of 13 objects is  $5.1 \times 10^{-12}$ , assuming a random distribution, a probability of 0.0641 for a single trial (based on a search radius of  $0''.5$  and the total field of view of the WFPC2), and using a binomial probability distribution (i.e.,  $[n! \times (n-m) \times p^{m(1-p)}] / [(n-m)! \times m!]$ ; where  $n$  is the number of trials,  $m$  is the number of matches, and  $p$  is the probability of a match in a single trial). However, this approach underestimates the probability since the sources are not distributed randomly over the full field of view. A more realistic estimate can be made by performing Monte-Carlo calculations by offsetting the optical sources by small spatial offsets (i.e., using a grid with delta-X and delta-Y in the range  $\pm 5''$ , with  $1''$  increments), and then searching for matches. This preserves the large-scale distribution of the sources. Figure 2 shows that the mean number of predicted random matches is 2.18, which translates to a probability of 0.168 for a single trial. The curve in Figure 2 shows the predicted probability using the binomial formula and  $P=0.168$ . It is in good agreement with the results from the Monte-Carlo calculation, giving us confidence in an extrapolation to larger numbers of matches than is practical to obtain using the Monte-Carlo calculations. The predicted probability for 11 matches for 13 objects is  $4.6 \times 10^{-7}$ , according to the binomial formula. This clearly demonstrates that the  $1''.2$  offset is justified, and there are optical counterparts for nearly all of the bright thermal radio sources.

The only bright thermal radio sources that do not have matches are 1-3 and 4-4 (radio designations are from Table 5 of Neff & Ulvestad 2000). 1-3 is in a dust lane 5'' NW of the nucleus of NGC 4039. The radio source is relatively bright ( $S=303 \mu\text{Jy}$ ) and is atypical in the sense that it has the highest value of the radio index  $\alpha$  (+0.38) of the 13 galaxies. Radio source 4-4 is in a dust lane halfway between regions C and D (see Figure 5 of Whitmore et al. 1999), and can be seen as the circle closest to the North arrow in Figure 1 (*bottom*). It is also quite bright in the radio ( $S=680 \mu\text{Jy}$ ) and has a typical value of  $\alpha$  (–0.16). Taken at face value, this suggests that  $2/13 = 15\%$  of the bright thermal radio sources are embedded in sufficient dust to obscure their optical emission in the HST observations.

It will be important to observe the two undetected radio sources using high resolution IR observations, to determine whether they are obscured star clusters, and if so, whether they have properties similar to the detected radio sources. For example, if these clusters turn out to be amongst the intrinsically brightest clusters, it is possible that they may influence the luminosity function in important ways, even though there are relatively few missing clusters.

Similar enhancements in the number of matches are found for other subsets of the radio sample once the 1''2 offset is made. These subsets are listed in Table 1. In particular, 77% of the 13 very bright radio sources ( $S > 300 \mu\text{Jy}$ ) have optical counterparts, and 62% of the 45 bright sources ( $S \geq 70 \mu\text{Jy}$ ) have optical counterparts. However, when only the faint radio sources are used ( $S < 70 \mu\text{Jy}$ ), there is essentially no enhancement in the number of counterparts. This may indicate that the radio sources are associated with sources other



than star clusters. For example, it is possible that they arise from individual supernova remnants, which may not appear bright enough to be included by the  $M_I < -9$  selection criteria.

We note that only  $\sim 10$  % of the apparent  $U$  light from the Antennae stems from clusters (i.e., the fractions are 9/8/5/7 % for U/B/V/I respectively; the cluster-rich PC has the highest percentage of light in clusters with 16/22/15/21 %; the WF4 has the lowest with 4/3/2/3 %; and the overlap region is intermediate with 9/8/5/7 %). Similar fractions were found in NGC 3256 by Zepf et al. (1999). These fractions should be considered lower limits, since only clusters brighter than  $M_I = -9$  were included in the calculation. In addition, we assume that the extinction is the same in the clusters and in the field. Nevertheless, it appears that a majority of the  $U$  light comes from field stars rather than clusters. This might explain why most of the faint radio sources, apparently associated with individual supernova remnants, appear to be associated with the field rather than the clusters. We should also keep in mind that some of the weakest radio sources are likely to be noise rather than real sources, hence artificially reducing the number of matches for the faint sources.

Table 2 includes the 37 radio sources with good positional matches with the  $M_I < -9$  clusters (within  $0''.5$ ), once the  $1''.2$  offset is made. A Monte-Carlo calculation indicates that 13.8 matches would be expected if there were no correlation between radio and optical sources. This indicates that  $p=0.1265$  for a single trial. The chances of having 37 matches from the 109 radio sources is  $6.0 \times 10^{-9}$ , according to the binomial formula. Hence, based on statistics alone, we believe there is compelling evidence for an offset of  $1''.2$  between the

radio and optical image.

## *2.2 Astrometric Analysis*

Offsets of  $1'' - 2''$  are often seen in HST images, due to uncertainties in the guide star positions. Hence, in cases in which accurate astrometric positions are required, observers are urged to check for offsets in the WFPC2 positions by measuring the position based on measurements from the Digital Sky Survey (DSS), following the procedure described at: <http://www-gsss.stsci.edu/support/phase2.html> .

Unfortunately, the ground-based DSS image of the Antennae has only a few point-like objects in common with our HST images, since most of the DSS image is saturated. However, it is possible to measure a region to the NE of region D (see Figure 5a in Whitmore et al. 1999) on both the DSS image and the WFPC2 image. Using this cluster we find an offset of  $-0.036$  s (or  $-0''.51$ ) in RA and  $-1''.05$  in DEC. This is similar to our empirically determined values of  $-0.035$  s (or  $-0''.49$ ) in RA and  $-1''.07$  in DEC discussed in §2.1 . Expected accuracies for the DSS coordinates are  $\sim 0''.2 - 0''.3$ .

A final check is possible using a star on WF2 (i.e., star 2 in Figure 5b of Whitmore et al. 1999), which turns out to be an USNO astrometric reference (i.e., obtained from their archival web site at <http://www.nofs.navy.mil/data/FchPix/>). We find that the offset it implies for the HST images it is in very good agreement with our previous estimates (i.e.,  $-0.033$  s [or  $-0.47''$ ] in RA and  $-1.16''$  in DEC).

Hence, there is good evidence from both the statistics discussed in §2.1, and the

independent astrometric checks discussed in this section, that an offset with an amplitude of  $\sim 1''.2$  toward the SW is required to bring the WFPC2 image into alignment with the radio image. The good correlations between the radio and optical properties, discussed in §5, provide a final piece of confirming evidence for this offset.

### 3. IDENTIFICATION OF RADIO AND OPTICAL COUNTERPARTS

Having established that an offset of the HST coordinates  $1''.2$  to the southwest is required to bring the radio and optical images into alignment, we now attempt to identify specific matches. Figure 3 shows the locations of all 109 radio sources. The large circles show matches with bright thermal sources ( $S \geq 70 \mu\text{Jy}$ ,  $\alpha \geq -0.4$ ) while the large squares show matches with bright non-thermal sources ( $S \geq 70 \mu\text{Jy}$ ,  $\alpha < -0.4$ ). The small symbols are for the faint radio sources (i.e.,  $S < 70 \mu\text{Jy}$ ).

Each of the 37 matches was inspected in order to select the most likely optical counterpart, since there are many cases where more than one cluster is found within the search radius of  $0''.5$  from the radio position. During this process we noted a tendency for some of the radio source to be closer to strong  $H\alpha$  emission peaks than to bright sources which are not associated with  $H\alpha$ . Perhaps the best example is Knot S (near the top of Figure 4) which is optically the second brightest (apparent) cluster in the Antennae. The radio source does not appear to be associated with the cluster itself, but instead is found  $\sim 1''$  to the southeast, closer to several regions of strong  $H\alpha$ . In these cases we identified two possible counterparts, one where the brightest cluster in the circle was generally selected (in some cases a slightly fainter object was selected if it was much closer to the exact radio

position; see Appendix A), and one where the strongest  $H\alpha$  source was chosen. In some cases a strong  $H\alpha$  source just outside the search circle was selected. We will call the first sample the brightness-selected sample and the second the  $H\alpha$ -selected sample. A third sample, consisting of the 37 matches discussed above but using the total  $H\alpha$  flux within a radius of 0.5" (i.e., the “radio aperture”), has also been defined. This will be called the radio-position sample. In §5 we attempt to identify which is the more physically meaningful sample by examining the resultant scatter in various correlations. The three samples, along with their radio counterparts and other ancillary information, are listed in Table 3.

While the good correlations we find in §5 indicate that most of these radio-optical matches are probably correct, it should be kept in mind that based on statistics alone, some of the matches are likely to be misidentifications. Hence, caution is advised when making specific one-to-one matches. We also note that the intrinsic correlations will be better than indicated in §5, since the misidentifications will add noise.

#### 4. AGE DATING THE CLUSTERS

In §5 we will compare various radio and optical properties of the 37 radio sources with optical counterparts. In the present section we first fine-tune our age estimates for the clusters, since several properties we will use in these comparisons are derived from these determinations.

Whitmore et al. (1999) estimated ages for the clusters in the Antennae by comparing the UBVI colors with Bruzual & Charlot (1996) spectral evolution models. They found

evidence for five populations of clusters, ranging in age from  $\sim 1$  Myr to  $\sim 15$  Gyr. The middle panel of Figure 5 shows a  $U - B$  vs  $V - I$  diagram for the 37 radio sources with optical counterparts, along with the Bruzual & Charlot (2000) instantaneous burst spectral evolution models with solar metallicity (using their models with theoretical isochrones) as the solid line, and Starburst99 (Leitherer et al., 1999) models as a dotted line. The models are shown alone in the top panel, along with the Bruzual & Charlot (2000) models with empirical isochrones for comparison (dot-dashed lines). The positions for ages of 1, 5, 10, 100, and 1000 Myr for the BC00-theoretical models are shown in large numbers while the positions for 1, 6.5, 8 and 13 Myr for the Starburst99 models are shown in smaller numbers. The straight dashed lines show the reddening vectors due to obscuration by dust (Mathis 1990) for ages of 1, 5 and 10 Myr and the BC00 models with theoretical isochrones.

Some of the large differences between the Starburst99 models and the Bruzual & Charlot models are due to the dominating influence of cool red supergiants in the Geneva spectral evolution models used by Starburst99, relative to the Padova models used in the Bruzual & Charlot models. We note that of 37 objects, only cluster 984 lies in a position that would populate the prominent “red loop” (i.e., ages 8 - 13 Myr) seen in the Starburst99 models. The bottom panel of Figure 5 shows the distribution for the 100 (apparent) brightest clusters in the Antennae, where no clusters would populate the red loop. The Bruzual & Charlot models with theoretical isochrones appear to provide a better fit to the majority of the data, and hence will be used in the remainder of the paper. We note that a similar effect can be seen for the clusters in M83 (Harris et al. 2002; Figure 6).

Object 841 is the nucleus of NGC 4039, and sits in a position that would imply an age of  $\sim 1$  Gyr. This is likely to be caused by a combination of light from an old population ( $\sim 15$  Gyr), intrinsic to the pre-existing nucleus, and a young population of stars formed during the merger. The other clusters in this region of the diagram (3816, 2560, & 3475) appear to be normal star clusters. The most likely explanation for their position in the diagram is that they are young clusters heavily embedded in dust, since all three are found in the heart of the overlap region, where extensive dust is clearly apparent. This interpretation is strengthened by the fact that all three have relatively strong  $H\alpha$  emission, implying ages  $< 10$  Myr. We note that this would require the true reddening vector to be slightly steeper than the Mathis (1990) models used in the diagram. Finally, cluster 1139 (=WS80) is so red that it suffers from a severe red leak in the U filter, which artificially enhances the U magnitude. This is further discussed below.

#### *4.1 Breaking the Age-Reddening Degeneracy*

Our basic problem in determining ages is that for most clusters with  $A_V$  greater than about 1 mag, the reddening vector for a particular cluster intersects the models in two, or even three points, corresponding to two or three possible ages. For example, cluster 7453 has three possible ages;  $\sim 1$ ,  $\sim 7$ , and  $\sim 40$  Myr, depending on how far up the reddening vector we need to backtrack. Each of the three ages would also imply a different value of  $A_V$ .

Fortunately, we can break this degeneracy by using the strength of  $H\alpha$  emission. Figure 6 shows the predicted values of the  $H\alpha$  equivalent width (EW, in  $\text{\AA}$ ) as a function of

age, based on solar metallicity, an instantaneous burst, and a Salpeter initial mass function extending from 1.0 to 100  $M_{\odot}$  (Starburst99 models in Leitherer et al., 1999). For ages less than 4.8 Myr (where the curves in the  $U - B$  vs  $V - I$  diagram take a sharp turn as the red giants begin to dominate, resulting in the first level of degeneracy), the clusters should have  $\log H\alpha > 2.65$ , according to the models. By 8.7 Myr, where the next bend appears in the  $U - B$  vs  $V - I$  diagram resulting in the second level of degeneracy,  $\log H\alpha$  has dropped to 1.2. This is lower than the observed value in 36 of the 37 radio sources with optical counterparts, the only exception being object 841, which is probably the nucleus of NGC 4039. This object has been removed from the subsequent analysis. Hence, we can use the  $\log H\alpha = 2.65$  criterion to identify whether the cluster belongs in the 1 – 5 or the 5 – 9 Myr age range. None of the radio-optical matches appear to have larger ages. Once the correct age is known we use the difference between the apparent and intrinsic values of  $V - I$  to determine the extinction,  $A_V$ .

Values of  $H\alpha$  have been measured using the F685N observations from Whitmore et al. (1999). The  $H\alpha$  flux (using a conversion value of  $4.2 \times 10^{-15}$  erg/s/cm<sup>2</sup> for 1 DN/s; from [http://www.stsci.edu/instruments/wfpc2/Wfpc2\\_faq/wfpc2\\_nrw\\_phot\\_faq.html](http://www.stsci.edu/instruments/wfpc2/Wfpc2_faq/wfpc2_nrw_phot_faq.html)) was determined using a scaled version of the I band image to subtract the continuum. Although the offset in wavelength between  $H\alpha$  and the I band is non-optimal, this technique works well enough for our purposes since  $H\alpha$  is a steep function of age (see Figure 6), so small uncertainties can be tolerated. The I-band image is then used to estimate the value of the continuum and convert the  $H\alpha$  flux to equivalent width, using the values of photflam from Table 28.1 of the Data Handbook (Voit 1997). A small correction is made for the difference

in extinction between  $H\alpha$  and the I-band using Mathis (1990). Figure 6 shows that the data follow the predicted curve relatively well.

#### 4.2 Correcting the Colors for the Presence of $H\alpha$

Several practical issues need to be considered before final values for the ages can be determined. The first is the fact that the  $V$  observations are contaminated by the presence of strong hydrogen (4861 Å) and oxygen emission lines (4959 and 5007 Å), as demonstrated by Stiavelli et al. (1998) and also shown in Figure 16 of Whitmore et al. (1999). We have determined the correction for this effect by using the  $B - V$  vs  $V - I$  diagram, since the age and reddening vectors are nearly parallel for this combination of colors. This simplifies the problem by allowing us to solve for just two parameters rather than three (i.e., age, reddening, and contamination from emission lines). Figure 7 shows the raw  $B - V$  vs  $V - I$  diagram, with the ten clusters with the highest values of  $\log H\alpha$  (used as a surrogate for emission in the 4861, 4959, and 5007 Å lines) shown as open circles. As expected, these points tend to fall to the left of the models. Figure 8 shows the residuals from the 1 Myr BC00 models vs.  $\log H\alpha$ . We choose the 1 Myr models for reference since the clusters with large values of  $\log H\alpha$  are all very young (see Figure 6). Also note that the reddening lines for all ages less than 5 Myr are nearly identical in the  $B - V$  vs  $V - I$  diagram.

We correct for the  $\log H\alpha$  dependence of  $V - I$  using the equation:

$$(V - I)_{cor} = (V - I)_{apparent} + 2.5 \times \log [(1.4 \times 10^{-4} \times H\alpha) + 1] \quad (1)$$

and correct for the dependence of  $B - V$  using the equation



$$(B - V)_{cor} = (B - V)_{apparent} - 2.5 \times \log [(1.1 \times 10^{-4} \times H\alpha) + 1], \quad (2)$$

where  $H\alpha$  is measured as an equivalent width in  $\text{\AA}$ .

These formulae were obtained by zeroing out the mean value of the residual for the ten clusters with the highest values of  $H\alpha$ . Figure 8 shows both the correlation and the resulting correction (dashed line) for  $B - V$ . Figure 9d shows the resulting  $B - V$  vs  $V - I(\text{cor})$  diagram after the correction has been made.

Another difficulty is introduced by the very red clusters, where large extrapolations are required. Any small uncertainty in the reddening law therefore results in large uncertainties in the age estimate. In addition, for extremely red objects, the red leak in the F336W filter becomes a problem (see Zhang, Fall, & Whitmore 2001 for a discussion). This is why cluster 1139, with  $V - I = 2.92$ , has a value of  $U - B$  which is completely off-scale when compared to its value of  $V - I$  (see Figure 5). The U measurement appears to be  $\sim 2$  magnitudes too bright, indicating that  $\sim 85\%$  of the light is coming from the red part of the spectrum rather than the UV light. Cluster 984 may also suffer from a redleak problem, which is partly compensated by the fact that this cluster has the highest value of  $H\alpha$ , making the cluster appear bluer in  $V - I$  than it should.

We deal with both of these problems by making age estimates based on the color-color diagram only for clusters with  $V - I < 1.2$ . For redder clusters we make a rough age measurement based on the strength of  $H\alpha$  emission alone.

#### *4.3 Combining Age Estimates*

Combining the age estimates based on the three different color-color diagrams is also problematic, since the uncertainties are often extremely non-linear (e.g., the 1 and 3 Myr reddening lines differ by only 0.04 mag in  $V - I$  at a constant  $U - B$  while the 7.2 and 8.7 Myr reddening lines differ by 0.51 mag). Table 3 includes a subjective “best guess” age estimate, based primarily on the  $U - B$  vs  $V - I$  diagram since it provides the most discriminating power, and using  $H\alpha$  to break the age-reddening degeneracy. Lesser weight is given to the other two color-color diagrams. For clusters that fall outside the possible age ranges predicted by the models (e.g., WS80 = 1139) we make rough age estimates based on  $H\alpha$ . A subjective quality rating, reflecting the consistency and availability of the various estimates, is included in Table 3. Figure 9 shows all four of the diagrams used to make the best guess estimate. The dashed lines show the reddening vectors for 1, 4.8, and 8.7 Myr.

A final caveat is suggested by the fact that the  $H\alpha$  measurements are made using the same apertures as the original UBVI measurements (i.e., a radius of 2 pixels for the PC and 1.5 pixels for the WF). However, for older clusters which have had time to blow superbubbles, most of the  $H\alpha$  emission associated with the cluster may be at larger radii (e.g., Knot S in Figure 4 has very little  $H\alpha$  within a 2 pixel radius). Hence, the  $H\alpha$  measurements should be regarded as lower limits. This does not appear to be a serious problem, however, since nearly all of the radio sources turn out to be associated with very young clusters where most of the  $H\alpha$  emission is still roughly coincident with the optical source.

## 5. CORRELATIONS BETWEEN RADIO AND OPTICAL PROPERTIES

Having established that most of the strong 6 cm radio sources have optical coun-

terparts, we are now able to study the sources in more detail. Figure 10 shows various correlations between radio and optical parameters. The significance of the correlation is included in the upper right of each diagram. Obvious outliers (labeled in Figure 10) have been removed before making the fits for Figures 10d and 10g. The eight sources with radio index  $\alpha < -0.8$  (i.e., non-thermal) are shown as open symbols. These sources generally follow the trends shown by objects with flatter radio indices, although two clusters (3816 and 10808) stand out as outliers in the  $\log H\alpha - A_v$  correlation (Figure 10g). We draw four conclusions from these diagrams.

First: There is a weak tendency for young clusters to be stronger radio sources (Figures 10a, 10b). This is not surprising since the UV radiation heating the gas is at its maximum for very young stars, as is the  $H\alpha$  EW which is controlled by the UV flux (Figure 6). This results in the good correlation between  $\log H\alpha$  and 6 cm radio continuum emission (Figure 10b), which has been well established by a number of past studies (e.g., Young et al. 1996).

We note the fan shaped correlation between  $\log H\alpha$  and  $\log S$  in Figure 10b (and in other diagrams such as 10f and 10g). This may indicate that the strongest radio sources are dominated by the single cluster that has been matched with it, while weaker radio sources may be associated with a different cluster, or perhaps with a combination of several clusters, hence adding noise to the correlation. This is discussed in another context at the end of this section.

Second: Based on Figure 10d, the radio sources with optical counterparts appear

to be primarily associated with objects with  $\alpha \geq -0.4$ , (i.e., thermal radio sources, Neff & Ulvestad 2000). This is demonstrated by the constant upper envelope consistent with a flat spectral index  $\alpha \approx -0.3$ . This is the same conclusion as reached in §2 based purely on statistical grounds. There is little or no correlation between the spectral index  $\alpha$  and any other parameters. Most of the scatter occurs toward steeper radio indices for fainter radio sources. These may represent a population of sources associated with supernova remnants, or may just represent misidentifications (i.e., noise). We also note that the source with the largest value of  $\alpha$  (cluster 5047 with  $\alpha = 1.0$ ) is also the faintest radio source, hence this may represent noise. This outlier was not included when making the fit to the data in Figure 10d.

Third: The younger clusters have the largest extinctions (Figure 10c, 10g). Based on the weak correlation shown in Figure 10c, it takes  $\sim 6$  Myr for a cluster to clear enough dust to reach  $A_V \sim 1$ . This is consistent with the trend found by Zhang, Fall, & Whitmore (2001), with a mean value of  $A_V \sim 1.5$  for the youngest B1 clusters ( $\leq 10$  Myr) and  $A_V \sim 0.3$  for the older B2 clusters ( $\geq 100$  Myr). We note that while we expect a good correlation between  $\log H\alpha$  and  $\log \text{Age}$ , Figure 10f cannot be used to independently prove this since it is largely built into the age-dating method (see §4).

Fourth: The strongest radio sources are also the intrinsically brightest clusters (Figure 10e). This is to be expected since the brightest optical clusters are likely to be the strongest UV sources, due to a combination of their relative youth (Figure 10f, 10h) and their higher luminosity. The weak trend between  $M_V$  and  $\log \text{Age}$  (Figure 10h) is due to the dimming

of the clusters with time, as predicted by the BC00 models (e.g., see Whitmore et al. 1997, Figure 13).

We can attempt to determine whether the radio sources are physically related to individual bright clusters, individual bright HII regions, or the mean  $H\alpha$  within a  $0''.5$  radius of the radio source by examining the degree of scatter in the various diagrams shown in Figure 10. Figure 11 shows the  $\log S$  vs.  $\log H\alpha$  diagram for all three samples defined in Table 3. (i.e., the brightness-selected,  $H\alpha$ -selected, and radio-position samples). There is essentially no difference between the brightness-selected sample and the  $H\alpha$ -selected sample. This is also true of the other seven correlations shown in Figure 10. However, the radio-position sample does show a difference, with a flatter slope and considerably less scatter (i.e., the RMS in  $\log H\alpha$  is 0.28, compared to 0.51 for the brightness-selected sample and 0.53 for the  $H\alpha$ -selected sample). The steeper correlation for the bottom two panels in Figure 11 is probably due to misidentifications of objects with clusters with weak  $H\alpha$ . From the top panel it would appear that essentially all of the radio sources with optical counterparts are strong  $H\alpha$  sources.

While the measurement of  $\log H\alpha$  in units of equivalent width is useful for our hybrid age determinations, the near constancy of  $\log H\alpha$  shown in Figure 11c, and the strong correlation between  $\log S$  and  $M_V$  (figure 10e), suggest that the underlying correlation may be with the total  $H\alpha$  flux within the “radio aperture”. Indeed, Figure 12 supports this interpretation, showing that the correlation between  $\log H\alpha$  (flux) and  $\log S$  for the radio-position sample is stronger ( $7.9 \sigma$ ) than between any of the other parameters for any of the

three samples.

## 6. WS80 - The Brightest Cluster in the Antennae

Whitmore et al. (1999) list Knot G (605 in Table 1 of Whitmore et al. 1999; see Figure 5 of that paper for location) as the brightest cluster in the Antennae, based on its apparent value of  $V$  (i.e.,  $M_V = -13.92$ , uncorrected for extinction). We note that this cluster is not a radio source, in agreement with its weak  $H\alpha$  (see Figure 4 of Whitmore et al. 1999). Mengel et al. (2001) estimate an age of 8 Myr for Knot G, older than our estimated ages for all but one of the radio-optical matches in Table 3.

However, now that we can determine values of  $A_V$  using the method described in §4, we find that cluster 1139 (# 3 in Tables 2 and 3) is the intrinsically brightest cluster in the Antennae, with  $M_V = -15.5$ , and a photometrically-determined mass of  $4 \times 10^6 M_\odot$  (i.e., assuming the values for luminosity and age from Table 2 and a BC00-theoretical model with solar metallicity; see Table 3 for the masses of other clusters). This cluster was originally identified by Whitmore & Schweizer (1995) as WS80, one of the very red objects that they suggested might be a young cluster still embedded in its dust cocoon.

Since then, WS80 has also been identified as the strongest CO source in NGC 4038/39 (Wilson et al. 2000), the strongest ISO source (Vigroux et al. 1996, Mirabel et al. 1998), and the strongest radio source (Neff & Ulvestad 2000, although they did not include the  $1''.2$  offset discussed in §2, and hence concluded that the true radio source was near but not coincident with WS80). Wilson et al. (2000) find that this is also the site of an apparent

collision between three giant molecular clouds.

WS80 is distinguished in our sample of 37 radio-optical matches as the cluster with the highest value of  $A_V$  (7.6 mag), the reddest color ( $V - I = 2.92$ , or 3.08 after using Equation 1), the third highest value of  $\log H\alpha$  (3.81), and one of the youngest ages ( $\sim 2$  Myr).

Figure 13 shows  $U, B, V, I, V/I$ , and  $H\alpha$  images of WS80 and WS355, two very red clusters identified at the end of Table 1 in Whitmore & Schweizer (1995). In both cases the clusters are nearly invisible in the  $U$  and  $B$  images, are faint in the  $V$  image, and are bright in the  $I$  image. This is in contrast to the blue clusters around them which are roughly the same brightness in all four colors. The contrast for the  $V/I$  image is adjusted to show the blue objects as black and the red objects as white. WS80 is the only red object in its field while there are two red objects in the WS355 field. Note the elongation and the knots of nebulosity around WS80. Most importantly, we find that WS80 is a strong  $H\alpha$  source, with the knots aligned with the red knots in the  $V/I$  diagram. In contrast, WS355 has essentially no  $H\alpha$  associated with it. This is presumably a somewhat older cluster which happens to have several magnitudes of extinction in front of it, hence we would not expect it to be a strong radio source. Mengel et al. (2001) estimated an age of 8.5 Myr for WS355, consistent with its lack of  $H\alpha$  emission (i.e., see Figure 6).

The identification of WS80 with the strongest radio, CO, and IR sources led to the expectation that many of the other very red sources may be similar objects (e.g., Wilson et al. 2000). However, we find no other object in Table 3 have  $(V - I)_{cor} > 2.0$ . In addition,

when we isolate the fifteen optical clusters in the overlap region with  $V - I > 2.0$ , and  $M_V < -9$ , we find that the only match with a radio source is WS80. If we instead isolate the eleven intrinsically brightest optical clusters in the overlap region with  $\log H\alpha > 3$ , we find 8 of the 11 clusters are radio sources (and two more would be if we allowed a  $1''$  radius criterion for radio-optical matches). Hence, it appears that the primary criteria required to produce strong radio sources are the intrinsic brightness of the cluster and the strength of its  $H\alpha$  emission. Very red clusters are *not* preferentially radio sources, contrary to earlier suggestions.

## 7. SUMMARY

A reexamination of the spatial correspondence between 6 cm continuum radio sources from Neff & Ulvestad (2000) and young clusters in the Antennae galaxies (Whitmore et al. 1999) leads to the following conclusions.

1. The HST image used in Whitmore et al. (1999) needs to be offset  $1''.2$  toward the southwest to bring it into alignment with the radio image. Determinations based both on maximizing the number of matches, and on a comparisons with independently determined positions of objects on the image give similar results. Offsets of this magnitude are not uncommon in HST images, due to uncertainties in the coordinate system of the guide stars. After the offset is made, 37 of the 109 radio sources have optical counterparts. The probability of this occurring from an uncorrelated sample is  $6.0 \times 10^{-9}$ .

2. Eight-five percent (11/13) of the strong thermal radio sources have optical coun-



terparts, indicating that only  $\sim 15\%$  of the sources are embedded in so much dust that they are not detected in the optical. Similar enhancements are found for the sample of very bright ( $S > 300 \mu\text{Jy}$ ) radio sources (10/13, 77 %), bright ( $S \geq 70 \mu\text{Jy}$ ) radio sources (28/45, 62 %) and bright non-thermal sources (16/31 = 52 %). Essentially no enhancement is found for the faint ( $S < 70 \mu\text{Jy}$ ; 8/64 = 12%) sources. One possible interpretation is that the faint sources, which are primarily non-thermal (i.e.,  $\alpha < -0.4$ ), arise from individual supernova remnants that are too faint to be seen in the visible. This might be explained by the fact that  $\sim 10\%$  of the UV light, and hence of the young star formation responsible for producing most of the supernovae, is associated with the field rather than the clusters.

3. A sample of 37 sources have been studied in detail, showing correlations between radio flux and a variety of optical characteristics, including cluster brightness,  $\text{H}\alpha$  flux and equivalent width,  $A_V$  extinction, and cluster ages. The strongest correlation ( $7.9 \sigma$ ) is between the radio flux and  $\text{H}\alpha$  flux (Figure 12). This relationship is probably the underlying cause behind several of the other correlations. The most luminous objects, in both the radio and optical, are young clusters with ages in the range 0 - 4 Myr and extinctions that range from  $A_V = 0.5$  to 7.6. In particular, the brightest radio source is also the intrinsically brightest optical cluster ( $\text{WS80} = 1139$ ). In addition, it is the strongest CO source as well as the strongest 15 micron source in the entire system. Furthermore, it has the highest extinction and is one of the youngest clusters in our sample of 37 radio-optical matches.

4. The radio bright phase lasts  $< 10$  Myr in our sample of clusters with radio-optical matches, as demonstrated by the fact that all 36 objects have strong  $\text{H}\alpha$  (i.e.,  $\log \text{H}\alpha > 1.5$ ).

This is consistent with the interpretation that most of the radio emission originates from hot thermal gas in compact HII regions. The gas is ionized by O and B stars which have lifetimes  $< 10$  Myr, hence the young ages for the radio sources. It appears that, on average, a 6 Myr old cluster has been able to disperse enough dust around it to reduce the value of  $A_V$  to about 1 mag.

5. The identification of WS80 with the strongest radio, CO, and IR sources led to the expectation that many of the other very red sources may have similar properties. However, only two of the 37 radio-optical matches have  $V - I > 2.0$ . In contrast, of the eleven intrinsically brightest optical clusters in the overlap region with  $\log \text{H}\alpha > 3$ , we find eight of the clusters are strong radio sources. Hence, while there is nearly a one-to-one correspondence between bright young clusters and radio sources, the very red clusters are *not* preferentially radio sources, contrary to earlier suggestions.

6. As part of this project we developed a hybrid technique for determining the ages of young star clusters, using a combination of *UBVI* photometry and  $\text{H}\alpha$  equivalent width to break the age-reddening degeneracy. We find that the Bruzual-Charlot (2000) models using the Padova spectral evolution tracks fit the data reasonably well, while the Starburst99 (Leitherer et al., 1999) models using the Geneva tracks have an additional “red loop” that is inconsistent with the data.

This work was supported by NASA grants GO-05416.01-93A and GO-07468.01-A. We thank Eddie Bergeron for the suggestion to use the DSS image to check the position

of the WFPC2 image, and for help with the probability calculations. We thank Bernhard Brandl for raising the question of whether the radio sources have optical counterparts during IAU symposium # 207, since this led us to look into this question more closely, resulting in this publication. We also thank Adrienne Lancon for a useful discussion, and Francois Schweizer, Michael Fall, and Bernhard Brandl for comments on the paper. Finally, we thank an anonymous referee for several useful comments.

**APPENDIX A - Notes to Table 2**

2-2: There are several clusters near or within the search radius. Adopted 1161 ( $V = 21.52$ ,  $V - I = 0.83$ ,  $R = 0.48''$ ) since it was closer to the radio position than the brighter cluster 1143 ( $V = 21.14$ ,  $V - I = 0.76$ ,  $R = 0.69''$ ).

2-4: There are several very bright clusters nearby. Adopted 1298 since it was the brightest ( $V = 19.07$ ,  $V - I = 0.67$ ,  $R = 0.32''$ ).

4-2: On the edge of region C (see Whitmore et al. 1999). Adopted the brightest object (2002,  $V = 19.06$ ,  $V - I = 0.14$ ), which is  $0.66''$  from the radio position. The closest object was 2033 ( $V = 20.96$ ,  $V - I = 0.33$ ,  $R = 0.19''$ ).

4-5: On the edge of region D. Adopted the brightest object (2410,  $V = 18.70$ ,  $V - I = 0.13$ ), which is  $0.49''$  from the radio position. The closest object was 2399 ( $V = 21.69$ ,  $V - I = -0.04$ ,  $R = 0.30''$ ).

4A-16: There are three bright clusters in the circle. Adopted the brightest object (5105  $V = 20.58$ ,  $V - I = 0.52$ ), which is  $0.29''$  from the radio position.

4A-9: There are several bright clusters just outside the circle, including 3772 ( $V = 20.58$ ,  $V - I = 1.39$ ;  $R = 0.81''$ ).

4B-2: Adopted the brightest cluster (3069,  $V = 20.92$ ,  $V - I = 0.21$ ), which is  $0.46''$  from the radio position. The closest object was 3003 ( $V = 23.2$ ,  $V - I = 0.81$ ,  $R = 0.45''$ ).

5-5: There are two good candidates in the circle. Adopted the redder object which is slightly closer to the radio position (7894,  $V = 20.74$ ,  $V - I = 0.99$ ,  $R=0.26''$ ), but the radio source is probably a combination with 7811 ( $V = 19.38$ ,  $V - I = 0.30$ ,  $R = 0.42''$ ).

7-2: Centered on part of the dust lane near the nucleus of NGC 4038. Adopted the very bright cluster 9089 ( $V = 18.51$ ,  $V - I = 0.07$ ) which is just outside the search radius ( $R = 0.71''$ ), but the true source may be embedded. The closest object was 9182 ( $V = 22.10$ ,  $V - I = 0.88$ ,  $R = 0.31''$ ).

9-4: There are several candidates in the circle. Chose the brightest cluster (5047,  $V = 21.59$ ,  $V - I = 0.26$ ,  $R = 0.25''$ ).

10-1: There are several candidates in the circle; the radio source may be the sum of several of them. Adopted the brightest cluster (5981,  $V = 19.63$ ,  $V - I = 0.27$ ,  $R = 0.36''$ ).

11-2: Near the very bright region S (8191,  $V = 17.60$ ,  $V - I = 0.30$ ,  $R=1.08''$ ), but have adopted object 6665 ( $V = 20.04$ ,  $V - I = -0.15$ ,  $R = 0.40''$ ) since it is much closer to the radio position and is a stronger  $H\alpha$  source.

13-7: Two roughly equal candidates. Adopted 11623 ( $V = 20.82$ ,  $V - I = 0.63$ ,  $R = 0.46''$ ) since it is slightly brighter than 11584 ( $V = 21.20$ ,  $V - I = 0.73$ ,  $R = 0.48''$ ).

## REFERENCES

- Biretta, J. et al. 2001, WFPC2 Instrument Handbook, Version 6.0 (Baltimore: STScI), 210
- Bruzual A. G., & Charlot, S. 1996, private communication
- Bruzual A. G., & Charlot, S. 2000, private communication
- Harris, J., Calzetti, D., Gallagher, J. S., Conselice, C. J., & Smith, D. A. 2002, AJ, 122, 3046
- Kunze D. et al. 1996, A&A 315, L101
- Leitherer, C., Schaerer, D., Goldader, J. D., González Delgado, R. M, Robert, C., Foo Kune, D., de Mello, D. F., Devost, D., & Heckman, T. M. 1999, ApJS, 123, 3 (Starburst99)
- Mathis J. S. 1990, ARA&A, 28, 37
- Mengel, S., Lehnert, M. D., Thatte, N., Tacconi-Garman, L. E. & Genzel, R. ApJ, 2001, 550, 280.
- Mirabel, L. F., Vigroux, L., Charmandaris, V., Sauvage, M., Gallais, P., Tran, D., Cevarsky, C., Madden, S. C., Duc, P.-A. 1998 A&A 333, L1
- Neff, S. G. & Ulvestad, J. S. 2000, AJ, 120, 670
- Stiavelli, M., Panagia, N., Carollo, M., Romaniello, M. Heyer, I., Gonzaga, S. 1998, ApJL, 492, L135
- Toomre, A. 1977, in The Evolution of Galaxies and Stellar Populations, edited by B.M. Tinsley and R. B. Larson (Yale University Press, New Haven), p. 401
- Vigroux, L. et al. 1996, A&A, 315, L93

Voit, M. 1997, HST Data Handbook (Baltimore: STScI)

Young, J. S., Allen, L., Kenney, J. D. P., Lesser, A. & Rownd, B. 1996, AJ, 112, 1903

Whitmore, B. C., Miller, B. W., Schweizer, F., & Fall, S. M. 1997, AJ, 114, 1797

Whitmore, B. C., & Schweizer, F. 1995, AJ, 109, 960

Whitmore, B. C., Zhang, Q., Leitherer, C., Fall, S. M., Schweizer, F. & Miller, B. W.

1999, AJ, 118, 1551

Wilson, C. D., Scoville, N., Madden S. & Charmandaris, V. 2000, ApJ, 542, 120

Zhang, Q., Fall, M. & Whitmore, B. C. 2001, ApJ, 561, 727

### FIGURE CAPTIONS

Figure 1 - Positions of the strong ( $S \geq 70 \mu\text{Jy}$ ) thermal ( $\alpha \geq -0.4$ ) radio sources (Neff & Ulvestad 2000) superposed on the F814W HST image of the overlap region. The top panel shows the original positions while the top panel (1b) shows the positions when the HST image is moved  $1''.2$  toward the southwest. An area in the upper right (Knot B) is shown with a factor of 10 diminution in Figure 1b in order to show more detail in a region that would otherwise be saturated.

Figure 2 - The probability of having a given number of matches for 13 trials. The histogram shows the results of a Monte-Carlo simulation, as described in the text. The curve is a binomial probability determined by the mean number of predicted matches. The number of matches using the original positions (3) is consistent with being from a random distribution while the 11 matches resulting after the  $1''.2$  offset has been made has a probability of  $4.6 \times 10^{-7}$ , based on the binomial probability.

Figure 3 - Locations of all radio sources from Neff & Ulvestad (2000) superposed on the HST F814W image (shifted  $1''.2$  to the southwest). The circles are thermal sources ( $\alpha > -0.4$ ); the squares are non-thermal sources ( $\alpha < -0.4$ ). Large symbols are for the bright sources ( $S > 70$ ); small symbols are for the faint sources ( $S < 70$ ).

Figure 4 - Locations of radio sources in part of the western loop, after the  $1''.2$  offset has been applied to the HST images. The left panel (4a) is the F814W image, the right panel (4b) is the  $\text{H}\alpha$  image (with the F814W continuum subtracted). The large circles show the  $0''.5$  search radius around the radio source. The small circles show the candidates from the “brightness-



selected” sample while the small squares show the candidate from the “H $\alpha$ -selected sample. Note that the very bright cluster near the top of Figure 4a (Knot S; near cluster candidates 8064 and 8086) is not a radio source, but the region of strong H $\alpha$  below Knot S (Figure 4b) is a radio source.

Figure 5 -  $U - B$  vs  $V - I$  diagram with data points from the 37 optical counterparts (middle panel) from the brightness-selected sample. The solid curve is the Bruzual-Charlot (2000) model using theoretical isochrones; the dot-dashed curve is the Bruzual-Charlot (2000) model using empirical isochrones; and the dotted curve is the Starburst99 (Leitherer et al., 1999) model, all for solar metallicity. The straight dashed lines show the reddening vectors for ages 1, 5, and 10 Myr from the Bruzual-Charlot (2000) models with theoretical isochrones and Mathis (1990) reddening law. Various clusters are identified and discussed in the text. The bottom panel shows the corresponding diagram for the 100 brightest (apparent) clusters in the Antennae. Note that there are almost no clusters in the region of the diagram that would be populated by the “red loop” in the Starburst99 models (i.e., ages 8 – 13 Myr).

Figure 6 -  $\log H\alpha$  vs.  $\log \text{Age}$ . The curve shows a Starburst99 (Leitherer et al., 1999) model for an instantaneous burst, solar metallicity model (i.e., their Figure 45). The adopted ages are the “best guess” values, as discussed in the text.

Figure 7 -  $B - V$  vs  $V - I$  diagram with data from the 37 optical counterparts in the brightness-selected sample. The curve shows the Bruzual-Charlot (2000) model using theoretical isochrones; the dashed lines show the Mathis (1990) reddening vectors for ages 1, 5, and 10 Myr, which are nearly parallel with the age models. The ten clusters with the largest values of H $\alpha$  are shown using open circles, demonstrating how the presence of emission lines

(4861, 4959, 5007 Å) in the  $V$  passband affect the broadband color determinations.

Figure 8 -  $B - V$  residuals from the 1 Myr reddening vector in Figure 7 as a function of  $\log H\alpha$ . The dashed line shows the curve (Equation 2) used to correct for the presence of emission lines in the  $V$  passband for the subsequent analysis. See text for details.

Figure 9 - The four figures used to estimate the “best guess” age estimates for the clusters.  $B - V(\text{cor})$  and  $V - I(\text{cor})$  have been corrected for the presence of emission lines in the  $V$  passband, as discussed in the text. The dashed lines show the Mathis (1990) reddening vectors for ages 1, 4.8 and 8.7 Myr. The open circles show the data for cluster 5105. While multiple ages are possible based on the color-color diagrams, the strong  $H\alpha$  strength indicates that an age  $\sim 3$  Myr is the correct answer.

Figure 10 - Eight plots showing the correlations between various radio and optical properties for the brightness-selected sample. The solid circles are for sources with  $\alpha > -0.8$  while the open circles are for sources with  $\alpha < -0.8$  (i.e., non-thermal). The significance of each correlation is shown in the upper right corner of the panel. Obvious outliers (labeled) have been removed from Figures 10d and 10g before making the fits.

Figure 11 - The  $\log S$  vs.  $\log H\alpha(\text{EW})$  diagram for the three samples described in the text. Note that the scatter is much smaller in the radio-position sample, suggesting that the primary correlation is with  $H\alpha$  flux rather than equivalent width.

Figure 12 - The  $\log S$  vs.  $\log H\alpha$  (flux) diagram for the radio-position sample. The resulting correlation ( $7.9 \sigma$ ) is stronger than between any other parameters for any of the three samples. Hence, the relationship between the total  $H\alpha$  (flux) and radio flux ( $S$ ) is probably the

underlying correlation which is responsible for many of the other trends (e.g., Figure 10a, 10b, 10e).

Figure 13 -  $U$ ,  $B$ ,  $V$ ,  $I$ ,  $V/I$ , and  $H\alpha$  images of the regions around WS80 (cluster 1139) and WS355 (cluster 7086), two very red clusters identified by Whitmore & Schweizer (1995). The contrast for the  $V/I$  image is adjusted to show the blue objects as black and the red objects as white. Note that WS80 is a strong  $H\alpha$  source while WS355 has essentially no  $H\alpha$  associated with it. This explains why WS355 is not a radio source.

Table 1: Number of Radio-Optical Matches for Various Subsets

Sample	no offset	with 1''2 offset
All radio sources	25/109 (22 %)	37/109 (34 %)
Very Bright ( $S > 300 \mu\text{Jy}$ )	6/13 (46 %)	10/13 (77 %)
Bright ( $S \geq 70 \mu\text{Jy}$ )	14/45 (31 %)	28/45 (62 %)
Faint ( $S < 70 \mu\text{Jy}$ )	11/64 (17 %)	8/64 (12 %) <sup>a</sup>
Bright, thermal ( $S \geq 70 \mu\text{Jy}, \alpha \geq -0.4$ )	4/13 (31 %)	11/13 (85 %)
Bright, non-thermal ( $S \geq 70 \mu\text{Jy}, \alpha < -0.4$ )	9/31 (29 %)	16/31 (52 %)
Faint, thermal ( $S < 70 \mu\text{Jy}, \alpha \geq -0.4$ )	1/15 (7 %)	2/15 (13 %)
Faint, non-thermal ( $S < 70 \mu\text{Jy}, \alpha < -0.4$ )	10/49 (20 %)	6/49 (12 %)

Note to TABLE 1

<sup>a</sup> Monte-Carlo calculations indicate that a random sample with a spatial distribution similar to the radio sources will result in 13.8/109 matches (13 %). This is essentially what is found for the faint ( $S < 70 \mu\text{Jy}$ ) sources. See text for details.

Table 2: Matches between Radio and Optical Positions

#	HST ID <sup>a</sup>	Radio ID	RA <sup>b</sup> (h:m:s)	DEC <sup>b</sup> (d:':")	$\Delta$ RA <sup>c</sup> (")	$\Delta$ DEC <sup>c</sup> (")	V <sup>d</sup> (mag)	V-I <sup>d</sup> (mag)	S <sup>e</sup> (mJy)	$\alpha^e$	$\pm$
(1)	(2)	(3)	(4)	(5)	(6)	(7)	(8)	(9)	(10)	(11)	(12)
1	841	1-2	12:01:53.52	-18:53:10.50	-0.10	0.05	18.00	1.29	513	-0.63	0.14
2	984	1-4	12:01:53.35	-18:53:07.90	0.16	-0.24	22.48	1.40	365	-0.2	0.21
3	1139	2-1	12:01:54.96	-18:53:06.10	0.08	-0.02	23.52	2.92	5161	-0.26	0.13
4	1161	2-2	12:01:54.52	-18:53:05.40	-0.08	-0.47	21.52	0.83	241	-0.52	0.38
5	1298	2-6	12:01:54.58	-18:53:03.40	0.31	-0.07	19.07	0.67	2257	-0.3	0.13
	(1300) <sup>f</sup>				-0.18	-0.05	19.03	0.34			
6	1321	2-4	12:01:55.37	-18:53:02.80	-0.03	-0.16	21.95	0.70	63	-0.45	0.5
7	2002	4-2	12:01:55.34	-18:52:49.20	0.37	-0.55	19.06	0.14	1215	-0.98	0.13
8	2349	3-7	12:01:54.58	-18:52:43.90	-0.01	0.16	23.46	1.14	89	-1.03	0.37
9	2410	4-5	12:01:55.71	-18:52:42.80	0.48	0.11	18.70	0.13	243	-0.74	0.19
10	2560	4-7	12:01:55.14	-18:52:40.60	0.17	0.11	22.54	1.24	616	-0.37	0.18
11	3069	4B-2	12:01:56.03	-18:52:35.50	-0.04	0.46	20.92	0.21	43	-0.65 <sup>e</sup>	0.76
	(3050) <sup>f</sup>				0.36	0.26	21.50	0.09			
12	3367	4A-4	12:01:54.94	-18:52:32.40	-0.22	-0.12	21.87	0.79	61	-1.27 <sup>e</sup>	0.69
13	3475	4A-6	12:01:54.74	-18:52:31.70	0.31	-0.07	22.64	1.84	341	-0.36	0.15
14	3816	4A-9	12:01:55.25	-18:52:29.50	0.20	-0.42	22.34	1.56	76	-1.67 <sup>e</sup>	0.65
15	4411	8-2	12:01:51.95	-18:52:27.30	-0.31	0.28	19.66	0.42	113	-0.41	0.29
16	5047	9-4	12:01:50.88	-18:52:24.60	0.18	0.17	21.59	0.26	32	1.04	0.7
17	5105	4A-16	12:01:55.41	-18:52:24.30	-0.27	0.11	20.58	0.52	262	-0.38	0.24
18	5308	4A-15	12:01:55.57	-18:52:23.70	0.06	0.22	20.31	0.66	88	...	...
19	5981	10-1	12:01:50.46	-18:52:21.20	-0.32	0.17	19.63	0.27	217	-1.27	0.32
	(5875) <sup>f</sup>				0.66	-0.23	20.84	0.26			
20	5946	8-4	12:01:52.13	-18:52:21.10	0.11	-0.04	20.25	0.44	198	0.18	0.18
21	6665	10-2	12:01:50.26	-18:52:18.80	0.30	0.27	20.04	-0.15	49	-0.28	0.6
	(6593) <sup>f</sup>				-0.10	0.01	22.37	0.49			
22	7342	11-1	12:01:50.81	-18:52:16.20	0.28	0.25	21.00	0.22	102	-0.46	0.32
23	7453	5-4	12:01:54.91	-18:52:15.30	-0.04	-0.18	22.42	0.98	76	0.02	0.37
	(7527) <sup>f</sup>				0.40	0.12	22.70	0.81			
24	7894	5-5	12:01:54.82	-18:52:13.60	0.26	-0.04	20.74	0.99	120	-0.42	0.28
25	8036	11-2	12:01:50.45	-18:52:13.10	-0.30	-0.01	21.32	0.49	355	-0.77	0.22
	(8064) <sup>f</sup>				-0.60	0.08	21.00	0.26			
26	8416	5-7	12:01:54.66	-18:52:11.80	0.25	0.11	18.87	0.03	74	-0.23	0.4
	(8469) <sup>f</sup>				-0.13	0.31	20.27	0.01			
27	9162	5-9	12:01:54.54	-18:52:08.60	0.00	0.16	19.20	-0.06	88	-0.19	0.34
28	9089	7-2	12:01:53.01	-18:52:08.50	-0.61	-0.37	18.51	0.07	145	-0.58	0.2
29	9344	7-5	12:01:53.05	-18:52:06.80	0.42	-0.29	21.10	0.80	204	-0.52	0.2
30	9569	12-1	12:01:50.46	-18:52:05.50	-0.37	0.16	19.09	0.12	80	-0.35	0.34
	(9494) <sup>f</sup>				0.08	-0.29	20.95	0.08			
31	9896	7-8	12:01:53.02	-18:52:02.30	0.17	-0.07	19.80	0.84	1354	-0.48	0.13
32	10285	6-1	12:01:54.58	-18:51:56.70	0.15	-0.16	21.26	0.90	493	-0.65	0.16
33	10808	13-3	12:01:51.32	-18:51:49.50	-0.22	-0.36	20.03	1.15	59	-1.21 <sup>e</sup>	0.69
34	10937	13-4	12:01:51.28	-18:51:48.50	0.02	-0.10	22.76	0.70	47	-0.81 <sup>e</sup>	0.74
35	11623	13-7	12:01:51.35	-18:51:43.30	-0.42	-0.19	20.82	0.63	43	-0.65 <sup>e</sup>	0.76
36	12340	13-9	12:01:51.95	-18:51:38.60	0.13	0.20	21.90	0.86	191	-0.45	0.2
37	12532	13-10	12:01:52.62	-18:51:37.40	0.28	0.24	19.75	0.12	71	-1.55 <sup>e</sup>	0.67

## Notes to TABLE 2

<sup>a</sup> Based on full list of  $\sim 14,000$  point sources (including both clusters and stars) from Whitmore et al. (1999), placed in order of ascending RA. Note that this system is being introduced in the current paper; the numbers do not match the ID numbers used in earlier papers. A full list of the new ID numbers, cross referenced with the old list, is available on request by contacting the author.

<sup>b</sup> Radio positions from Neff & Ulvestad (2000).

<sup>c</sup> In the sense, radio – HST position.

<sup>d</sup> From Whitmore et al. (1999). Uncorrected for extinction.

<sup>e</sup> From Neff & Ulvestad (2000). Values marked with <sup>e</sup> are upper limits.

<sup>f</sup> Values in parenthesis are from the H $_{\alpha}$ -selected sample. See text for details.

Table 3: Various Parameters for Radio-Optical Matches

- 38 -

#	HST ID	Radio ID	(V-I) <sub>cor</sub> <sup>a</sup> (mag)	A <sub>V</sub> (mag)	M <sub>V</sub> <sup>b</sup> (mag)	log H <sub>α</sub> <sup>b</sup> (EW)	log H <sub>α</sub> (radio) <sup>b,c</sup> (EW)	Age (Myr)	Quality <sup>d</sup> (log M <sub>⊙</sub> )	Mass <sup>e</sup>
(1)	(2)	(3)	(4)	(5)	(6)	(7)	(8)	(9)	(10)	(11)
2	984	1-4	1.75	4.33	-13.26	3.87	3.50	2.	2	5.7
3	1139=WS80	2-1	3.08	7.62	-15.51	3.81	3.17	2.	2	6.6
4	1161	2-2	0.94	2.09	-11.97	3.10	3.52	3.7	1	4.9
5	1298	2-6	0.94	2.16	-14.50	3.52	3.39	3.8	1	5.9
	(1300) <sup>f</sup>		0.76	1.88	-14.26	3.71	3.39	2.	2	6.1
6	1321	2-4	1.09	1.65	-11.12	3.66	3.54	2.	1	4.9
7	2002	4-2	0.52	1.28	-13.62	3.60	3.52	2.	1	5.9
8	2349	3-7	1.39	2.03	-9.99	3.47	3.61	2.	1	4.4
9	2410	4-5	0.23	0.02	-12.73	2.83	3.52	3.	2	5.3
10	2560	4-7	1.40	3.45	-12.32	3.40	3.35	2.	3	5.3
11	3069	4B-2	0.42	0.40	-10.89	3.23	3.56	2.	1	4.8
	(3050) <sup>f</sup>		0.60	1.48	-11.39	3.78	3.56	2.	2	5.0
12	3367	4A-4	1.02	2.52	-12.06	3.47	3.58	4.8	2	5.0
13	3475	4A-6	2.09	5.17	-13.93	3.77	3.57	2.	2	6.0
14	3816	4A-9	1.58	3.91	-12.98	2.51	2.62	5.	3	5.4
15	4411	8-2	0.49	0.30	-12.05	2.72	3.23	6.	2	5.0
16	5047	9-4	0.31	0.77	-10.60	2.59	3.09	5.2	1	4.4
17	5105	4A-16	0.68	1.36	-12.19	3.18	3.17	2.5	2	5.2
18	5308	4A-15	0.67	0.82	-11.92	1.82	2.79	7.4	1	5.1
19	5981	10-1	0.31	0.33	-12.12	2.42	3.13	6.4	1	5.1
	(5875) <sup>f</sup>		0.58	1.43	-12.00	3.54	3.13	2.	2	5.2
20	5946	8-4	0.80	1.97	-13.13	3.65	3.62	2.	2	5.7
21	6665	10-2	-0.12	0.00	-11.37	2.38	3.07	4.5	1	4.7
	(6593) <sup>f</sup>		0.90	2.23	-11.27	3.74	3.07	2.	2	4.9
22	7342	11-1	0.32	0.16	-10.57	2.89	3.37	4.	1	4.3
23	7453	5-4	1.18	1.81	-10.80	3.35	3.41	7.	2	4.6
	(7527) <sup>f</sup>		1.36	3.36	-12.07	4.01	3.41	2.	2	5.2
24	7894	5-5	1.06	1.18	-11.85	2.77	3.17	8.4	2	5.2
25	8036	11-2	0.63	0.51	-10.60	3.06	3.31	7.	2	4.5
	(8064) <sup>f</sup>		0.45	1.12	-11.53	3.27	3.31	2.	2	5.0
26	8416	5-7	0.06	0.01	-12.55	2.37	3.02	4.	2	5.1
	(8469) <sup>f</sup>		0.24	0.58	-11.72	3.27	3.02	2.	2	5.1
27	9089	7-2	0.12	0.30	-13.21	2.56	3.33	5.	1	5.4
28	9162	5-9	0.10	0.90	-13.11	3.16	3.71	2.	2	5.6
29	9344	7-5	0.92	2.27	-12.58	3.14	2.00	4.8	1	5.2
30	9569	12-1	0.13	0.35	-12.67	2.02	2.96	5.2	1	5.2
	(9494) <sup>f</sup>		0.33	0.83	-11.29	3.37	2.96	2.	2	4.9
31	9896	7-8	1.05	2.24	-13.84	3.40	3.19	2.	2	6.0
32	10285	6-1	1.22	3.02	-13.16	3.69	3.71	2.	2	5.7
33	10808	13-3	1.15	1.95	-13.33	1.50	2.73	7.	1	5.6
34	10937	13-4	0.79	1.79	-10.43	2.98	3.06	6.	1	4.3
35	11623	13-7	0.65	0.59	-11.19	2.15	2.85	7.7	1	4.8
36	12340	13-9	1.26	3.11	-12.62	3.80	3.52	2.	3	5.5
37	12532	13-10	0.29	0.01	-11.67	3.10	3.39	2.	1	5.1

## Notes to TABLE 3

Object # 1 was omitted from the sample since it is the center of NGC 4039, rather than a cluster.

<sup>a</sup> Corrected for the presence of emission lines in the V band (see text). Uncorrected for extinction.

<sup>b</sup> Corrected for extinction.

<sup>c</sup> Log H<sub>α</sub> centered at the radio position, with a radius 0.5".

<sup>d</sup> 1 = highest quality (i.e., all 4 age indicators are in agreement) to 3 = lowest quality (i.e., some of the age indicators are in serious disagreement with other age indicators).

<sup>e</sup> "Photometric" mass determined from M<sub>V</sub>, Age, and the solar metallicity Bruzual & Charlot (2000) model. See text for details.

<sup>f</sup> Values in parenthesis are from the H<sub>α</sub>-selected sample. See text for details.

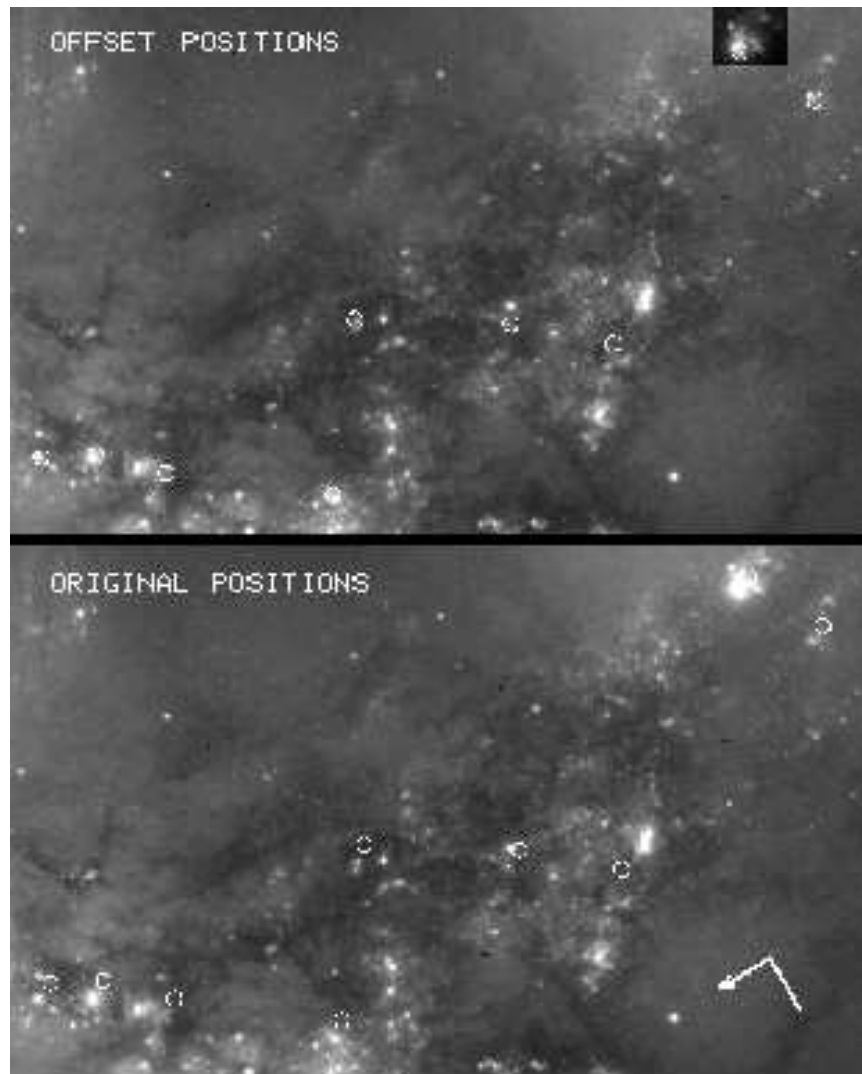


Fig. 1.—

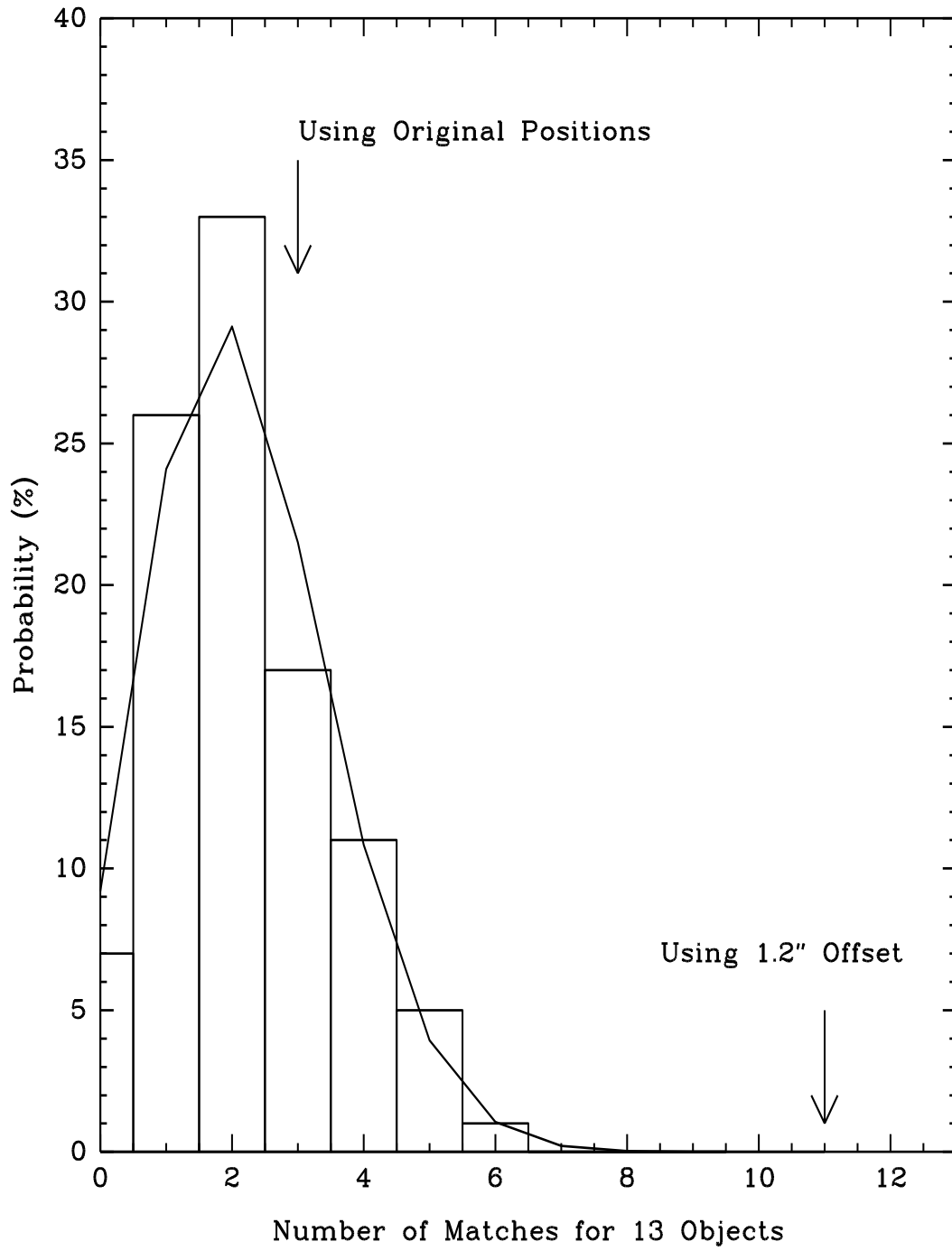


Fig. 2.—





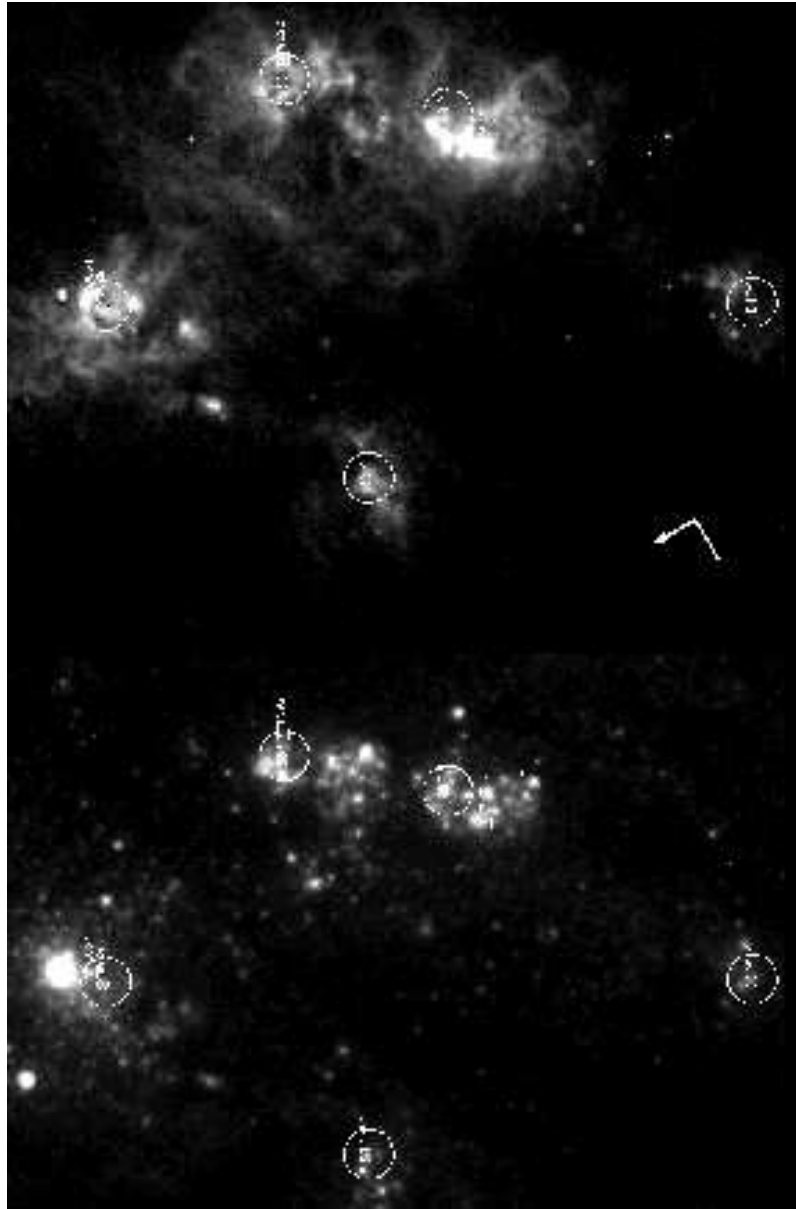


Fig. 4.—

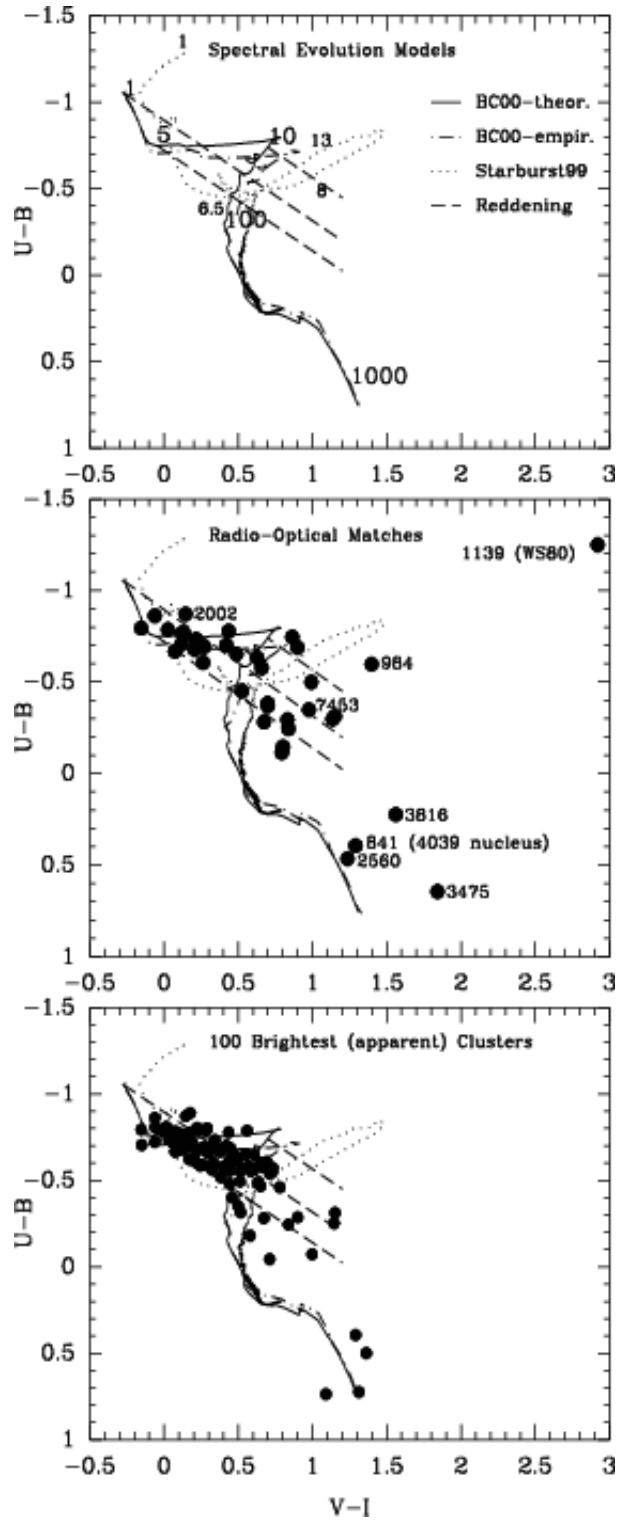


Fig. 5.—

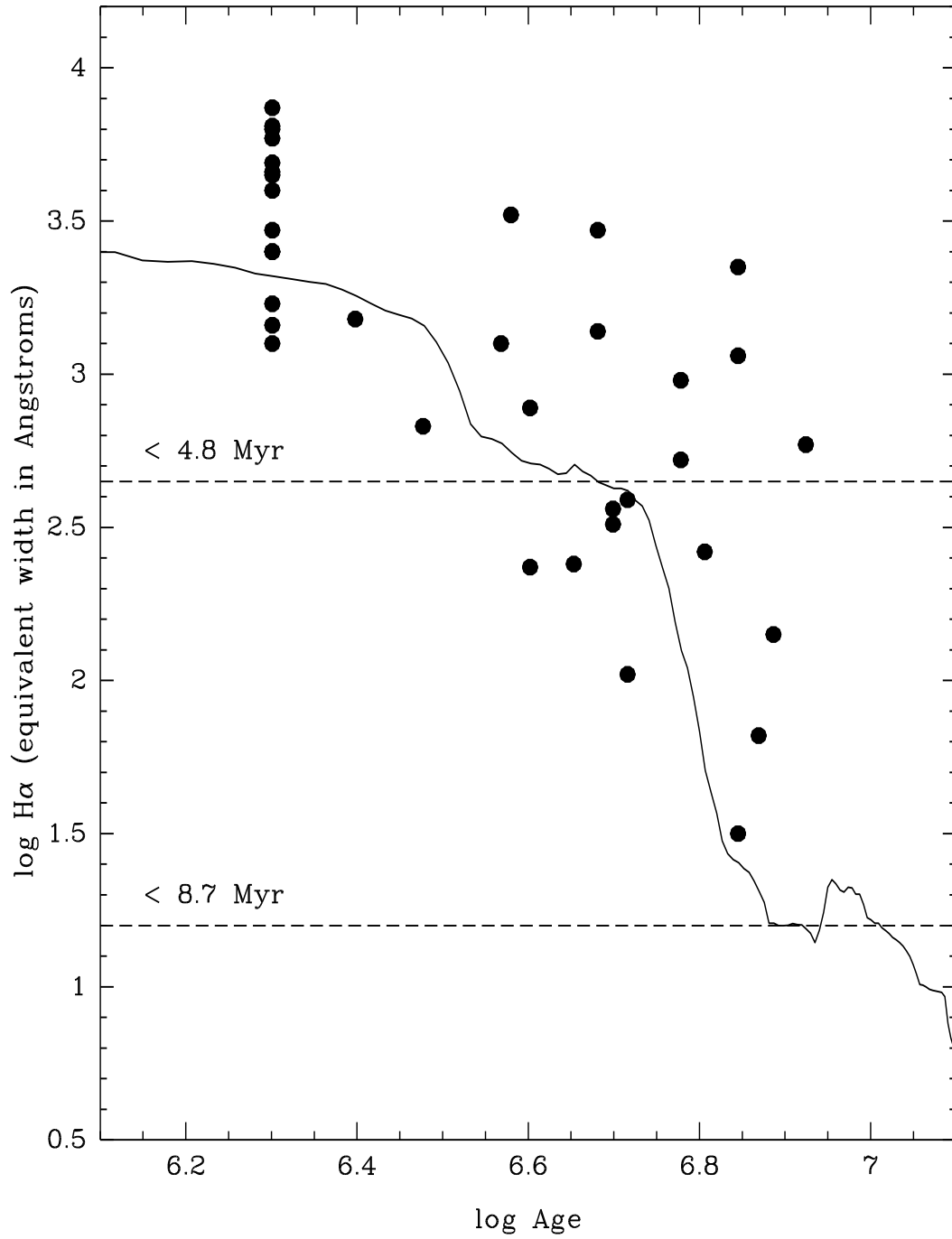


Fig. 6.—

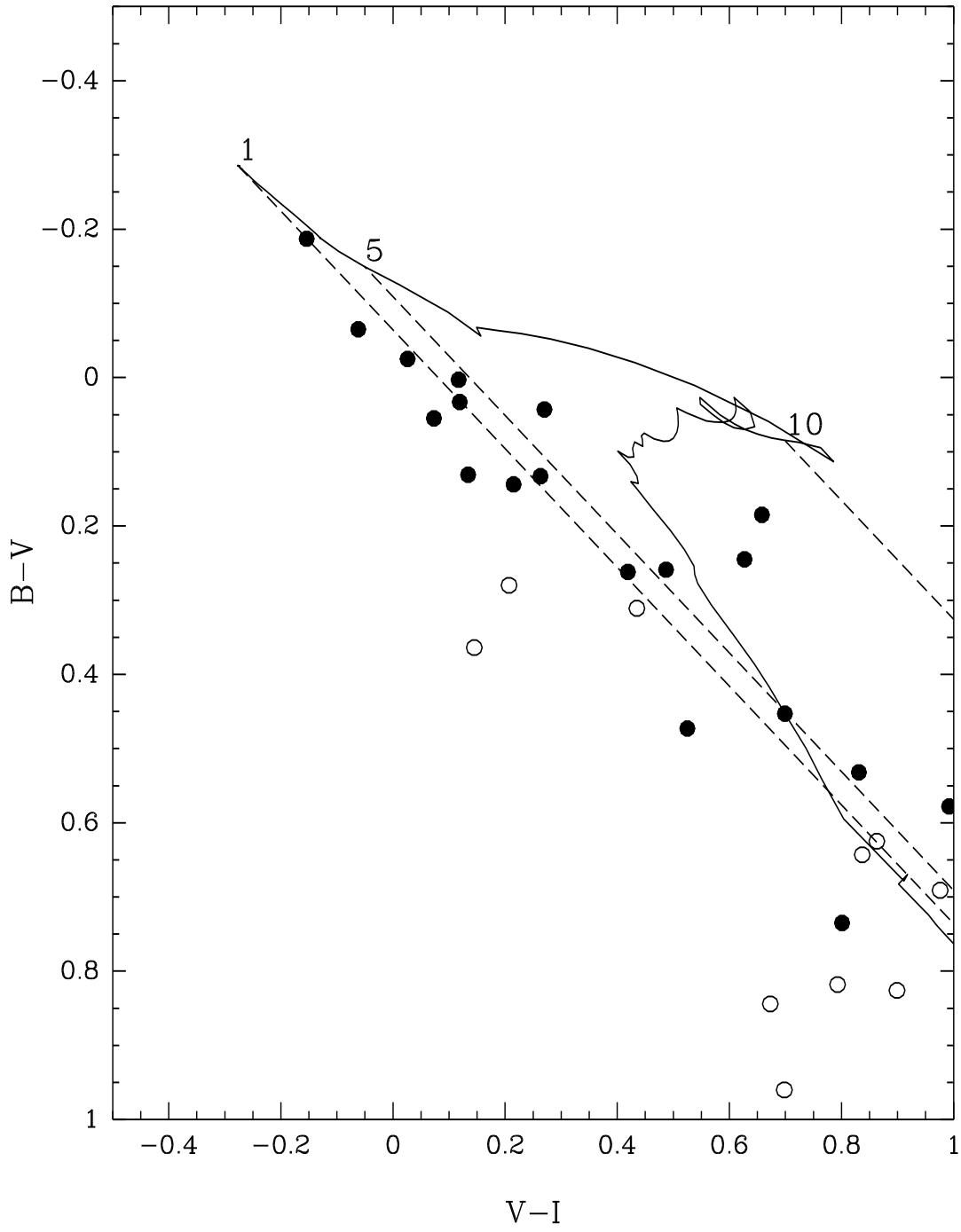


Fig. 7.—

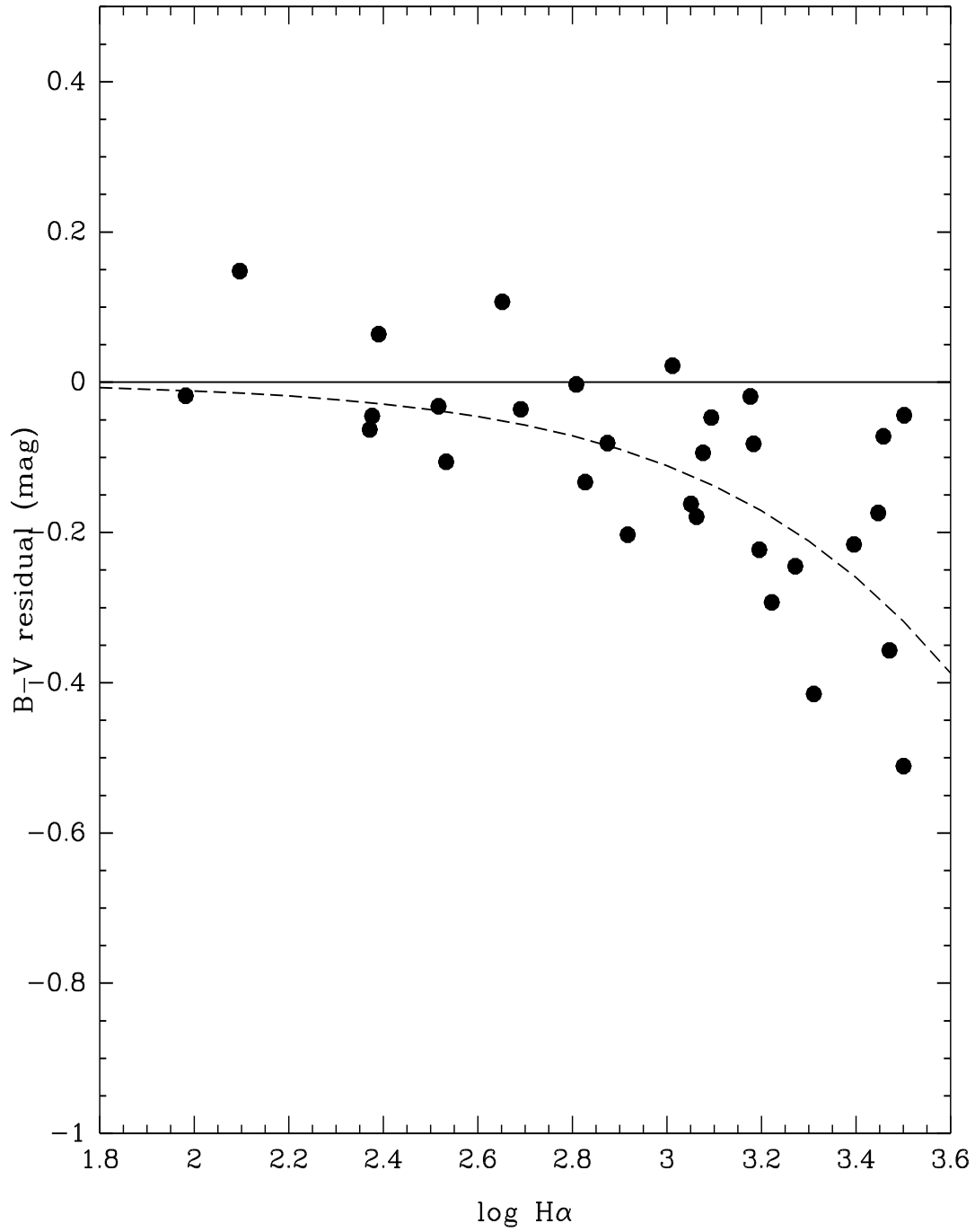


Fig. 8.—

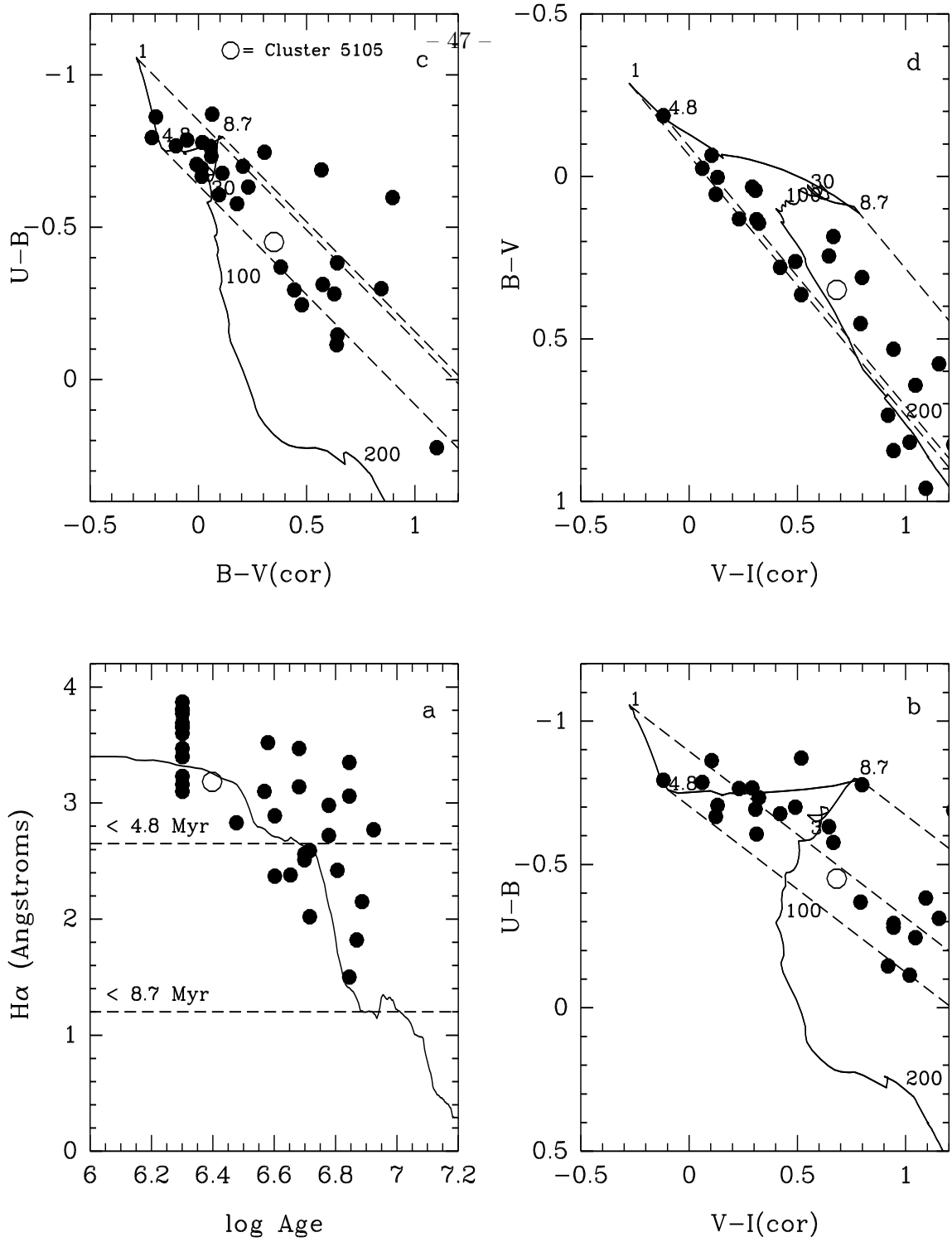


Fig. 9.—

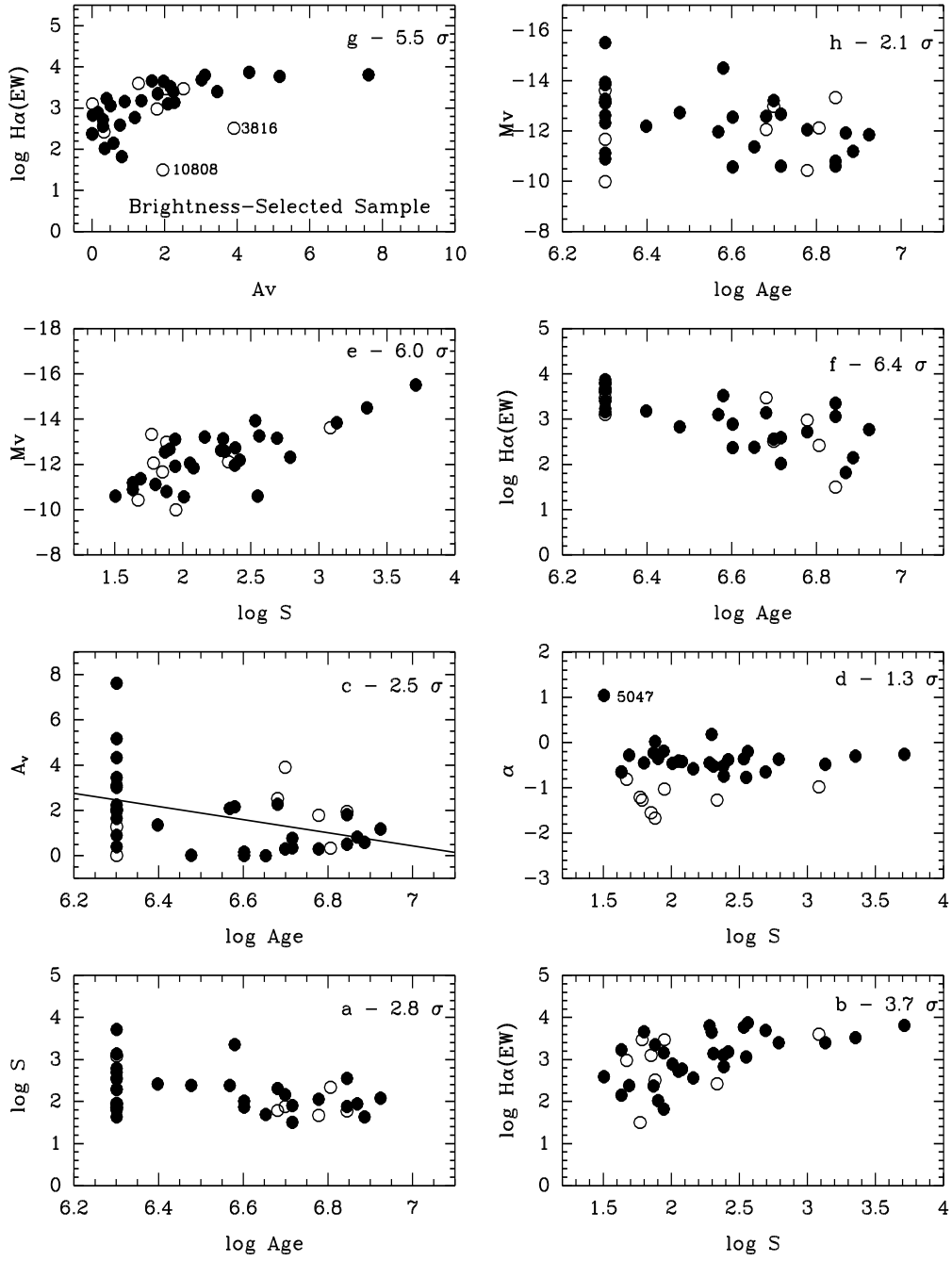


Fig. 10.—



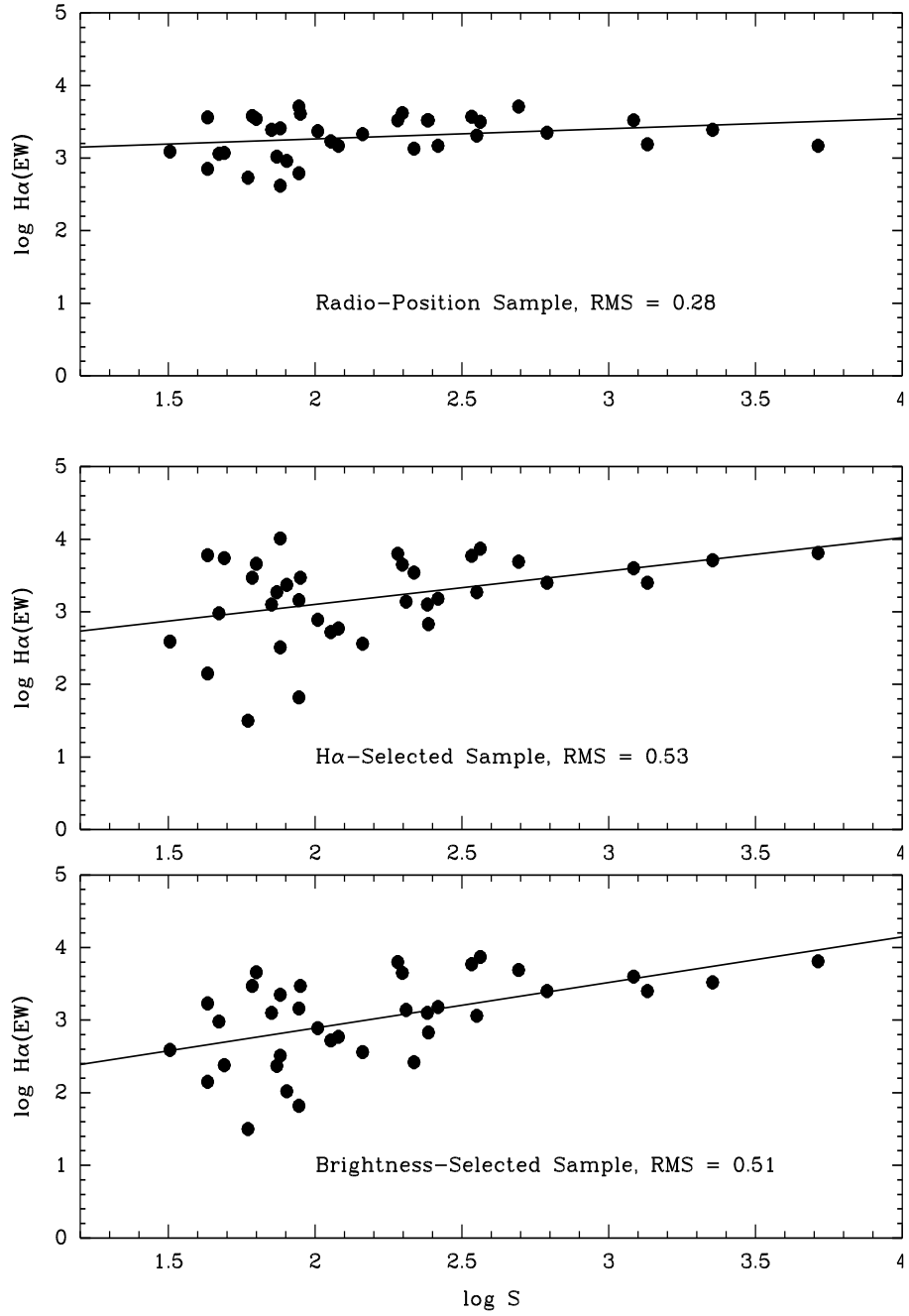


Fig. 11.—

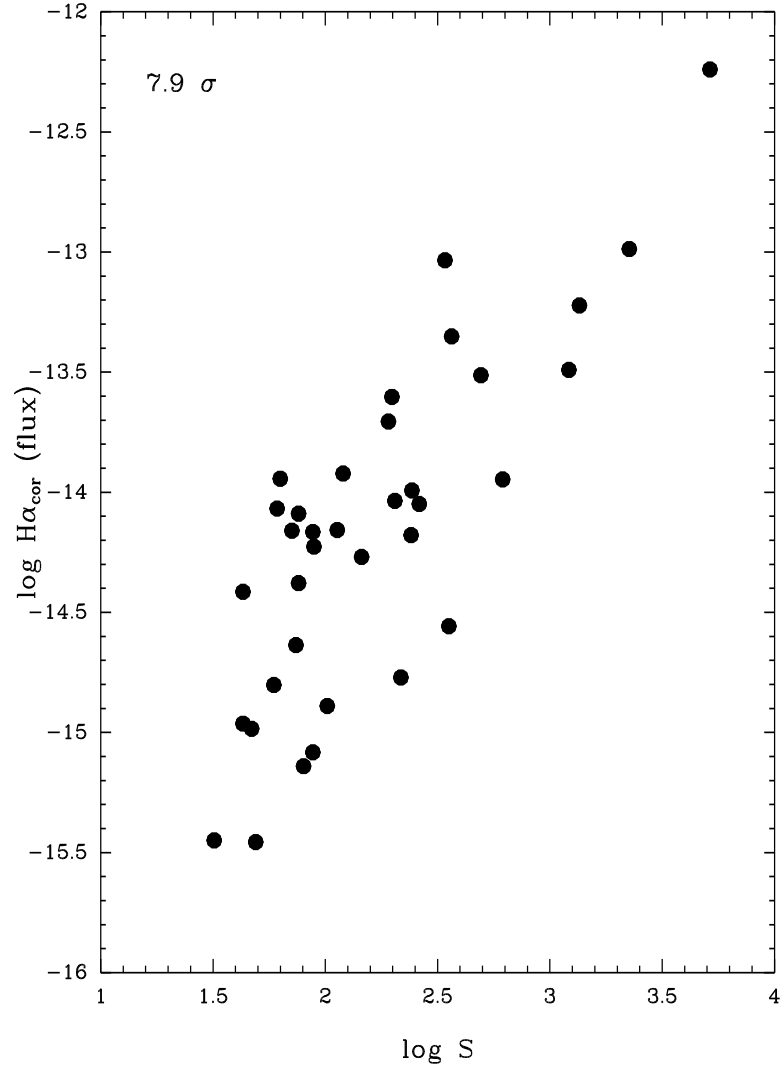


Fig. 12.—

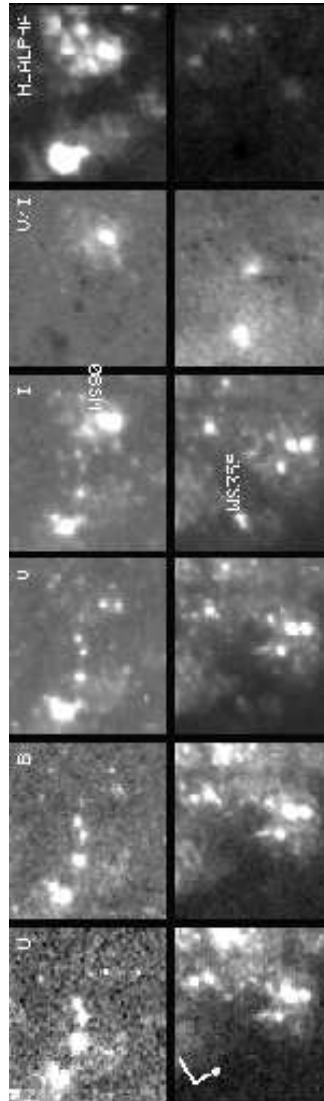


Fig. 13.—